ACS Catalysis
Research Article
pubs.acs.org/acscatalysis

Microstructure Effects on the Water Oxidation Activity of Co_3O_4/Porous Silica Nanocomposites

Chia-Cheng Lin, Yijun Guo, and Javier Vela*

Department of Chemistry, Iowa State University, and Ames Laboratory, Ames, Iowa 50011, United States

Supporting Information

ABSTRACT: We investigate the effect of microstructuring on the water oxidation (oxygen evolution) activity of two types of Co_3O_4/porous silica composites: Co_3O_4/porous SiO_2 core/shell nanoparticles with varying shell thicknesses and surface areas, and Co_3O_4/mesoporous silica nanocomposites with various surface functionalities. Catalytic tests in the presence of $Ru(bpy)_3^{2+}$ as a photosensitizer and $S_2O_8^{2-}$ as a sacrificial electron acceptor show that porous silica shells of up to ~20 nm in thickness lead to increased water oxidation activity. We attribute this effect to either (1) a combination of an effective increase in catalyst active area or consequent higher local concentration of $Ru(bpy)_3^{2+}$; (2) a decrease in the permittivity of the medium surrounding the catalyst surface and a consequent increase in the rate of charge transfer; or both. Functionalized Co_3O_4/mesoporous silica nanocomposites show lower water oxidation activity compared with the parent nonfunctionalized catalyst, likely because of partial pore blocking of the silica support upon surface grafting. A more thorough understanding of the effects of microstructure and permittivity on water oxidation ability will enable the construction of next generation catalysts possessing optimal configuration and better efficiency for water splitting.

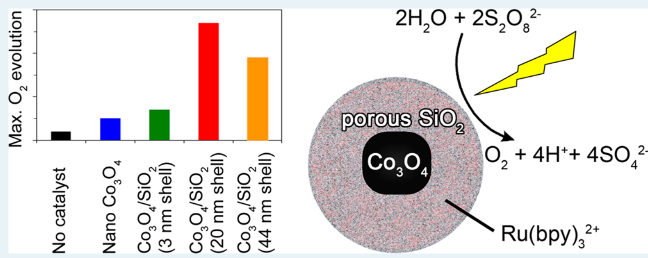

KEYWORDS: *Co_3O_4/SiO_2 core/shells, nanocomposites, nanocatalysts, water oxidation, microstructure effects*

INTRODUCTION

Electrochemical and photochemical water splitting are ways to produce molecular hydrogen gas, H_2, a potentially valuable and clean-burning fuel. Water oxidation is the most difficult half-reaction in water splitting, involving the transfer of four electrons and the formation of oxygen−oxygen bonds.[1−4] After many studies devoted to developing more efficient and economic water oxidation catalysts,[5] cobalt-based materials have been identified as some of the most promising due to their relative abundance, high activity, and stability.[2,6−8]

The synthesis and size-dependent properties of cobalt-based catalysts for electrochemical oxygen evolution have been examined previously.[9,10] A pH-dependent study of cobalt oxide electrocatalysts in fluoride buffer has been reported.[11] Cobalt oxide-decorated gold[12] or graphene[13] electrodes show some of the best catalytic performance in oxygen reduction and evolution reactions, whereas Co_3O_4-modified Ta_3N_5 photoanodes show enhanced performance and stability.[14,15] Co(II)-modified, fluorine-doped tin oxide has high catalytic activity,[16] as do self-repairing cobalt phosphate films[17] and diamond-supported Co_2O_3 nanoparticles.[18] Mesoporous Co_3O_4 prepared by hard-templating methods show increased stability and electrocatalytic ability.[19−21]

Several metal oxide-based photocatalytic systems in which the $[Ru(bpy)_3]^{2+}$ complex cation and $S_2O_8^{2-}$ serve as photosensitizer and sacrificial electron acceptor, respectively, have been developed. These include Mn_3O_4 embedded in mesoporous silica;[22,23] colloidal IrO_2;[24] MnO_2 nanotubes and wires;[25] amorphous manganese oxide;[26] MnO_2 on carbon nanotubes;[27] $LaCoO_3$, $CoWO_4$, $NdCoO_3$ and YCoO;[28] calcium manganese(III) oxide;[29] Mn−Ga−Co spinel;[30] cobalt/methylenediphosphonate;[31] $Li_2Co_2O_4$;[32] and $NiFe_2O_4$.[33]

Other than heterogeneous catalysts, homogeneous cobalt-based water oxidation catalysts that also require $[Ru(bpy)_3]^{2+}$ and $S_2O_8^{2-}$ have been developed. Carbon-free cobalt polytungstate complexes show improved stability and catalytic ability over traditional homogeneous water oxidation catalysts.[34−39] Water-soluble mononuclear cobalt complexes are converted into active $Co(OH)_x$ species during photocatalysis.[40] $Co(OH)_2$ derived from Co(II) adsorbed on silica shows high catalytic activity and stability.[41] Catalytic Co_4O_4 cubanes are known to mimic photosystem II.[42,43]

Water oxidation over mesoporous silica-supported Co_3O_4 clusters has drawn much recent interest.[44] The photo- and electrochemical activities of ligand-free Co_3O_4 nanoparticles of different shapes on different supports have been studied.[45] Co_3O_4/SBA-15 catalysts show higher activity than Co_3O_4/MCM41 catalysts.[46] Smaller Co_3O_4 clusters and 3-D connecting pore structures lead to better performance.[47] Mn-doped mesoporous Co_3O_4 performs better than pure Co_3O_4.[48,49] Cobalt complexes grafted on SBA-15, zeolite-supported CoO_x, and hollow Co_3O_4 particles have also been

Received: October 25, 2014
Revised: December 24, 2014
Published: December 24, 2014

reported.[50−54] The mechanism of hole transport from $[Ru(bpy)_3]^{2+}$ to the surface of Co_3O_4 was studied using Co_3O_4/SiO_2 core/shell catalysts impregnated with organic molecules as charge transfer media.[55,56]

Fundamental studies on the microscopic mechanism of water oxidation using both homogeneous (molecular) Co complexes[57] and heterogeneous Co_3O_4 catalysts[58] provide useful leads for new catalyst design and optimization. Theoretical calculations have described the adsorption and oxidation of water molecules on the $Co_3O_4(110)$ surface.[59] Here, we present our study on the effect of porous silica shell thickness and different surface grafted groups on the water oxidation activity of Co_3O_4/SiO_2 core/shells and Co_3O_4/mesoporous silica composites, respectively.

■ EXPERIMENTAL SECTION

Materials. Cobalt acetate tetrahydrate ($Co(OAc)_2{\cdot}4H_2O$), tetraethylorthosilicate (TEOS), Pluronic 123 (P-123, $HO(CH_2CH_2O)_{20}(CH_2CH(CH_3)O)_{70}(CH_2CH_2O)_2OH$), ammonium hydroxide ($NH_4OH$ 28 wt % aqueous solution), oxalic acid ($H_2C_2O_4$), cobalt(II) nitrate hexahydrate ($Co(NO_3)_2{\cdot}6H_2O$), poly(ethylene glycol) tridecamer ($HO(CH_2CH_2O)_{13}H$ (EG_{13} or PEG600), M_n = 600 g/mol), aminopropyltriethoxysilane ($H_2NCH_2CH_2CH_2Si(OEt)_3$), trimethylsilyl chloride (Me_3SiCl), tris(2,2′-bipyridyl)ruthenium(II) dichloride hexahydrate ($[Ru(bpy)_3]Cl_2{\cdot}6H_2O$), and deuterium oxide ($D_2O$) were purchased from Sigma-Aldrich; ethanol (absolute, 200 proof), ethylene glycol ($HOCH_2CH_2OH$; EG), and hydrochloric acid (HCl, concentrated) were from Fisher; cetyltrimethylammonium bromide (CTAB) was from Alfa Aesar; and phenyltrimethoxysilane ($PhSi(OMe)_3$) was from Gelest. All chemicals were used as received unless specified otherwise.

Synthesis. Co_3O_4 nanocrystals were prepared by a slightly modified procedure involving the thermal decomposition of cobalt(II) oxalate.[60] A solution of 0.3 M cobalt acetate in ethanol (50 mL) was heated and kept at 50 °C for 30 min, followed by quick addition of oxalic acid (1.07 g, 11.9 mmol). After 2 h at 50 °C, the cobalt(II) oxalate product was collected by concentration under vacuum at 80 °C. Heating cobalt(II) oxalate powder to 400 °C in a crucible in air for 2 h yielded Co_3O_4 nanocrystals.

Co_3O_4/porous SiO_2 core/shells. Co_3O_4 nanocrystals were coated with porous SiO_2 shells of varying thicknesses by modified literature procedures.[61−63] Co_3O_4 (50 mg, 0.21 mmol) was added to a mixture of CTAB (0.22 g, 0.60 mmol), 28 wt % aqueous NH_4OH (4.2 mL, 62.3 mmol), and ethanol (50 mL). After 15 min of sonication and 15 min of vigorous stirring, TEOS (25 μL, 0.11 mmol for 3 nm shell; 150 μL, 0.67 mmol for 20 nm shell; 600 μL, 2.64 mmol for 44 nm shell) was introduced in multiple small additions (<50−100 μL/h). The solution was stirred for 19 h at room temperature (RT). Solids were collect by centrifugation (5000 rpm, 10 min), and the surfactant was removed by calcination at 550 °C in air for 6 h.

Co_3O_4/SBA-15 nanocomposites. SBA-15[64] and Co_3O_4/SBA-15 nanocomposites[47,65] were prepared by modified literature procedures. P-123 (33 g, 5.69 mmol), concentrated HCl (16.6 g, 0.17 mol), and deionized water (517 g) were mixed by stirring vigorously at 35 °C for 30 min. TEOS (62.0 g, 0.30 mol) was added. After 1 day of stirring, the mixture was moved to an oven preheated to 90 °C and kept at this temperature for 1 day. Solids were collected by filtration and dried at 90 °C. The template was removed by calcination at 550 °C in air for 6 h. SBA-15 (0.2 g) was added to a 0.022 M cobalt(II) nitrate solution in ethanol (5 mL, 0.11 mmol), and the resulting pink slurry was stirred overnight until the solvent completely evaporated. This cobalt salt-impregnated SBA-15 was heated to 400 °C in air for 3 h. For surface grafting, Co_3O_4/SBA-15 composite (0.5 g) was degassed under vacuum at 110 °C for 2 h. Toluene (100 mL) and functional silane (44 mg of $H_2NCH_2CH_2CH_2Si(OEt)_3$, 40 mg of $PhSi(OMe)_3$, or 22 mg of Me_3SiCl; 2 mmol) were added. The mixture was refluxed at 78 °C under a dry N_2 atmosphere for 6 h. Solids were collected by filtration, washed with toluene (200 mL), and dried at 90 °C.

Structural Characterization. Powder X-ray diffraction (XRD) data were recorded with a Rigaku Ultima IV diffractometer with a Cu Kα radiation source (40 kV, 44 mA). Nitrogen physisorption was measured on a Micromeritics ASAP 2020 surface area and porosimetry system. Samples were degassed at 100 °C under vacuum overnight before analysis. The surface area was calculated with the Brunauer−Emmett−Teller (BET) method in the relative pressure range of 0.005−0.25 of adsorption data. Pore size distribution was calculated with the Barret−Joyber−Halenda (BJH) method. Transmission electron microscopy (TEM) was measured on an FEI Tecnai G^2 F20 field emission scanning transmission electron microscope (S/TEM) at 200 kV (point-to-point resolution < 0.25 nm, line-to-line resolution < 0.10 nm).

Spectroscopic Characterization. UV−vis absorption spectra were collected with a photodiode-array Agilent 8453 UV−vis spectrophotometer. Diffuse reflectance spectra were collected with a SL1 Tungsten halogen lamp (vis−IR), a SL3 Deuterium lamp (UV), and a BLACK-Comet C-SR-100 Spectrometer from StellarNet Inc.

Pore accessibility study. Co_3O_4/porous SiO_2 core/shell samples were examined by ^1H NMR spectroscopy using EG and polyethylene glycol ($HO(CH_2CH_2O)_{13}H$; Poly600). Experiments were conducted on a Varian MR-400 spectrometer equipped with a OneNMR pulse-field-gradient probe operating at a ^1H frequency of 399.80 MHz. EG (233 mg, 3.75 mmol) and Poly600 (317 mg, 0.53 mmol) were mixed in D_2O (5 g). A fraction of this EG/Poly600/D_2O solution (50 μL) and a solution of Co_3O_4/porous SiO_2 in D_2O (0.067 mM, 450 μL; 7.5 μg or 0.03 μmol of Co_3O_4) were mixed. NMR measurements of ethylene glycol and polyethylene glycol (Poly6oo) proton longitudinal (T_1) relaxation were conducted using the inverse recovery pulse sequence, and the transverse relaxation (T_2) was measured using a two-pulse spin echo sequence.

Solid state NMR spectra were measured with a Bruker Avance II 600 Spectrometer operating at 119.2 MHz for ^{29}Si equipped with a 4 mm Bruker MAS probe spinning at 10 kHz. ^{29}Si direct polarization magic angle spinning (DP-MAS) NMR spectra were recorded with a pulse width of 4 μs and a recycling delay of 1 min. ^{29}Si chemical shifts are referenced to TMS (δ = 0 ppm).

Water Oxidation. A buffer solution of weakly coordinating ions was prepared from $NaHCO_3$ (0.353 g, 4.20 mmol) and Na_2SiF_6 (0.619 g, 3.30 mmol) in deionized water (150 mL).[31] The pH was adjusted to 5.8 with added $NaHCO_3$. Buffer (20 mL), Na_2SO_4 (0.195 g, 1.37 mmol), $Na_2S_2O_8$ (65 mg, 0.27 mmol), $[Ru(bpy)_3]Cl_2{\cdot}6H_2O$ (22.5 mg, 0.03 mmol), and Co_3O_4/silica sample (1 mg or 4.2 μmol of Co_3O_4 for Co_3O_4/porous SiO_2 core/shells, determined by optical density in solution; 2 mg or 8.4 μmol of Co_3O_4 for Co_3O_4/SBA-15

DOI: 10.1021/cs501650j
ACS Catal. 2015, 5, 1037−1044

nanocomposites, determined by dry weight) were added to a 25 mL flask. The mixture was kept in the dark overnight and degassed by bubbling with dry N_2. O_2 evolution was unobserved by GC prior to illumination. Water oxidation experiments were conducted inside a Rayonet photoreactor under illumination with 16 × 575 ± 100 nm side-on lamps. Headspace samples (100 μL) were directly analyzed each time using an Agilent 7890A GC system equipped with a HP-Molesieve column and a TCD detector.

RESULTS AND DISCUSSION

Co_3O_4/Porous SiO_2 Core/Shells. Co_3O_4 nanocrystals were synthesized by thermal decomposition of cobalt(II) oxalate at 400 °C in air for 2 h (see the Experimental Section). As shown in Figure 1, the powder XRD pattern of the as-synthesized

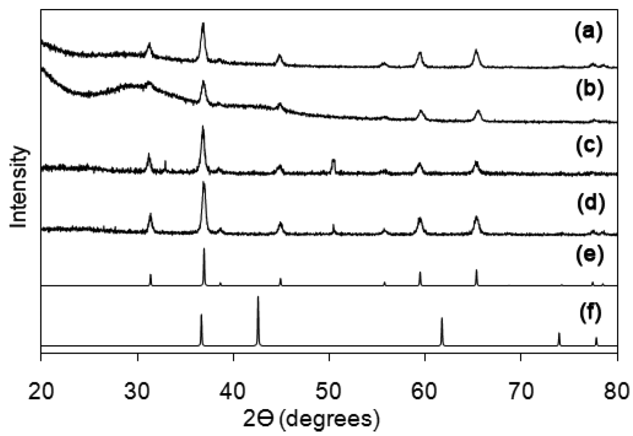

Figure 1. Wide-angle powder XRD data for 17.2 ± 3.8 nm Co_3O_4 nanocrystals (a); Co_3O_4/porous SiO_2 core/shell nanoparticles with different shell thicknesses of 3.1 ± 0.6 nm (b), 19.8 ± 1.4 nm (c), 44.1 ± 8.3 nm (d); and bulk Co_3O_4 (e) and CoO (f).

Co_3O_4 nanocrystals shows diffraction peaks that match those of the reference bulk spinel Co_3O_4 phase. In contrast, none of the experimentally observed diffraction peaks match those of bulk CoO, suggesting that the nanocrystals are made of highly phase-pure Co_3O_4. The diffuse reflectance spectrum of Co_3O_4 nanocrystals (Figure 2) shows two peaks at ~425 and 725 nm. This is consistent with the characteristic absorption of Co_3O_4, containing octahedral Co^{3+} and tetrahedral Co^{2+} ions.[66]

As shown in Figure 3, TEM shows that the Co_3O_4 nanocrystals have truncated polyhedral shapes with an average size (diameter) of 17.2 ± 3.8 nm. This is consistent with the grain size of 16 nm estimated from XRD peak widths using the Scherrer equation. Nitrogen physisorption analysis shows the specific surface area of Co_3O_4 nanocrystals is 38 m^2/g (Table 1), which is consistent with a surface area of 49 m^2/g estimated from a spherical particle model calculation. These Co_3O_4 nanocrystals were coated with porous silica (SiO_2) shells via CTAB-templated sol−gel condensation of tetraethylorthosilicate (TEOS) with NH_4OH as catalyst in ethanol solvent. TEM shows different amounts of TEOS resulted in different Co_3O_4/porous SiO_2 core/shell nanoparticles with various shell thicknesses (3.1 ± 0.6, 19.8 ± 1.4, and 44.1 ± 8.3 nm, Figures 1 and 3 and Table 1). The organic template, CTAB, was removed via calcination at 550 °C under air for 6 h.

Representative powder XRD, diffuse reflectance, and TEM data of Co_3O_4/porous SiO_2 core/shell nanoparticles are summarized in Figures 1, 2, and 3. As the silica shell becomes

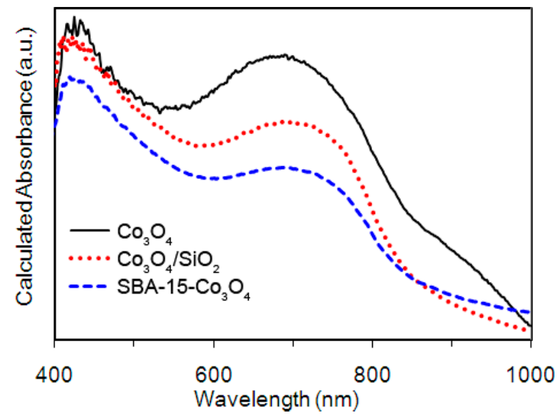

Figure 2. Diffuse reflectance spectra of bare (uncoated) Co_3O_4 nanocrystals (a), Co_3O_4/porous SiO_2 core/shell nanoparticles (19.8 ± 1.4 nm shell thickness) (b), and SBA-15-Co_3O_4 nanocomposites (4.4 ± 0.8 nm Co_3O_4 particle size) (c).

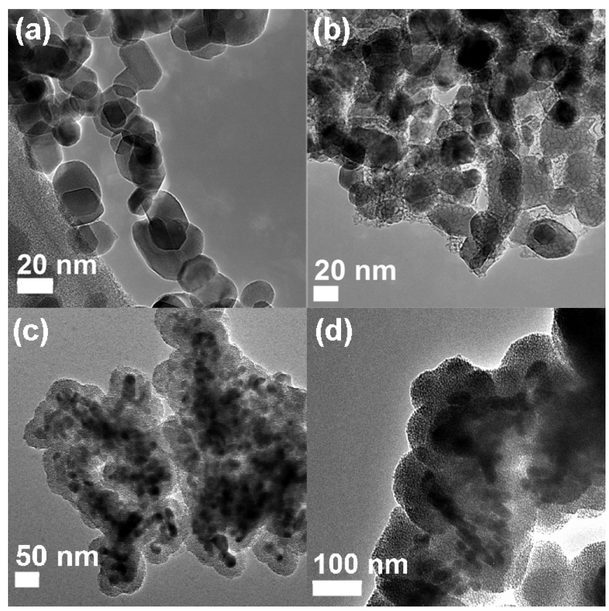

Figure 3. TEM of 17.2 ± 3.8 nm Co_3O_4 nanocrystals (a) and Co_3O_4/porous SiO_2 core/shell nanoparticles with different shell thicknesses of 3.1 ± 0.6 nm (b), 19.8 ± 1.4 nm (c), and 44.1 ± 8.3 nm (d).

Table 1. Structural Parameters of Co_3O_4/SiO_2 Core/Shell Nanoparticles with Different Shell Thicknesses

sample	core size (nm)[a]	shell thickness (nm)[a]	S_{BET} (m^2/g)[b]	pore size (nm)[c]	pore volume (cm^3/g)
Co_3O_4	17.2 ± 3.8	0	38	N/A	0.15
Co_3O_4/SiO_2 (3 nm)	19.1 ± 3.1	3.1 ± 0.6	130	N/A	0.15
Co_3O_4/SiO_2 (20 nm)	19.9 ± 3.0	19.8 ± 1.4	210	3.8	0.15
Co_3O_4/SiO_2 (44 nm)	24.1 ± 3.5	44.1 ± 8.3	390	3.9	0.22

[a]Determined by TEM. [b]Obtained by the BET method. [c]Obtained by the BJH method.

thicker, no significant peak shifts or new peaks are observed. The XRD patterns also reveal that the phase and grain size of

DOI: 10.1021/cs501650j
ACS Catal. 2015, 5, 1037−1044

the Co_3O_4 nanocrystals remain the same after silica coating, suggesting that the basic environment employed for silica coating does not affect the nanoparticles' Co_3O_4 cores. Similarly, no significant peaks appear in the low-angle XRD region (data not shown) of the Co_3O_4/porous SiO_2 core/shell nanoparticles. This implies that the porous silica shell may not be as ordered as other reported porous silica-coated materials that also use CTAB as a template or surfactant. In agreement with these XRD observations, diffuse reflectance and TEM confirm that the optical structure and size of the Co_3O_4 nanocrystals did not change appreciably through the silica shell growth process (Figure 3).

The average core size and shell thicknesses for different Co_3O_4/porous SiO_2 core/shell nanoparticles are summarized in Table 1. Increasing amounts of TEOS clearly resulted in larger shell thickness. This suggests that consecutive addition of TEOS resulted in the growth of (more) silica on pre-existing particles via heterogeneous nucleation, rather than forming new silica nuclei via homogeneous nucleation.

TEM reveals a foam-like surface structure is present atop the Co_3O_4/porous SiO_2 core/shell nanoparticles (Figure 3b−d). Nitrogen physisorption experiments were also performed to characterize the pore structure and surface area of the Co_3O_4/porous SiO_2 particles and their shells. The particles with 19.8 ± 1.4 and 44.1 ± 8.3 nm silica shells have calculated pore sizes of 3.8 and 3.9 nm, respectively, as obtained by the BJH method (see the Experimental Section, and Table 1). Core/shell particles with thinner silica layers did not show significant peaks by the BJH method. Across all samples studied, the specific surface area increased as the shell thickness increased. The pores in the silica shell are produced after the removal of CTAB molecules; the diameter of the pores is thus dictated by the size of the CTAB micelles formed during the sol gel process. Because the concentrations of CTAB, EtOH, and H_2O were the same in each run, the increase in surface area is consistent with increasing shell thickness while the pore size remains constant.

Probing Pore Accessibility by NMR. We then turned our attention to assessing the accessibility of the catalytically active Co_3O_4 surface to small molecules. While infrared spectroscopy provides one way to assess the degree of surface coverage by a silica shell,[67,68] we specifically sought to probe pore accessibility using nuclear magnetic resonance (NMR). NMR measurements of two chemically related molecules with very different sizes, ethylene glycol (EG) and polyethylene glycol tridecamer (EG_{13} or Poly600), were used to examine the pore accessibility of the Co_3O_4/porous SiO_2 core/shell nanoparticles. For all measurements, the concentration of ethoxyl protons (−O$\underline{CH_2}\underline{CH_2}$O−) in both EG and Poly600 were kept the same (confirmed by chemical integration), as was the concentration of (bare or coated) Co_3O_4 nanocrystals (confirmed by Co_3O_4 optical density or absorbance). Thus, only the thickness of the porous silica shells varied in different specimens.

Figure 4 shows the longitudinal (T_1) and transverse (T_2) relaxation times for the ethoxyl protons (−O$\underline{CH_2}\underline{CH_2}$O−) in EG and Poly600 in the absence and presence of Co_3O_4/porous SiO_2 core/shells. As expected, the T_1 values of EG and Poly600 do not change significantly with added Co_3O_4/porous SiO_2, regardless of the thickness of the silica shell (Figure 4a); however, the T_2 values for both EG and Poly600 progressively increase with increasing shell thickness (Figure 4b). Magnetic particles have been shown to be T_2 relaxers.[69] Studies with Fe_2O_3/SiO_2 core/shells showed that the thinnest shells have

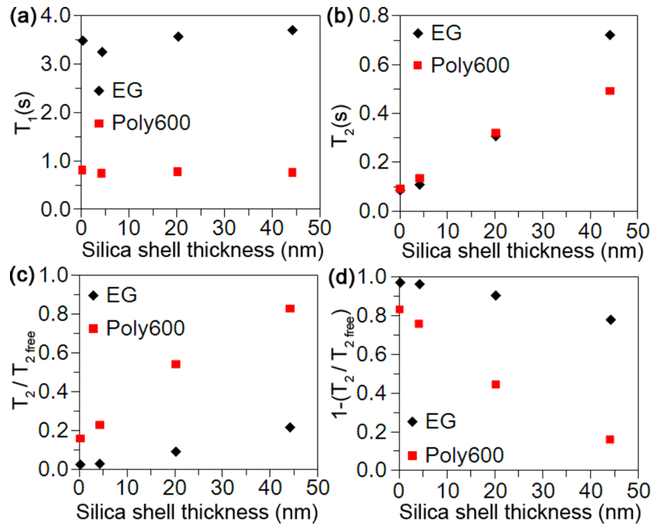

Figure 4. Longitudinal (T_1) (a) and transverse (T_2) (b, c, d) relaxation times for the ethoxyl protons (−O$\underline{CH_2}\underline{CH_2}$O−) in EG and Poly600 in the absence or presence of Co_3O_4/porous SiO_2 core/shell nanoparticles with different shell thicknesses in D_2O (T_{2free} = T_2 in the complete absence of Co_3O_4).

the strongest T_2 shortening effect.[70] A polymer-coated Fe_2O_3 composite shows enhanced T_2 shortening near the particle surface.[71]

Naturally, this shortening of the T_2 suggests that the magnetic Co_3O_4 core has a much larger influence on helping relax those protons that can get closer to the magnetic surface. It follows that thicker silica shells should increasingly separate and minimize the magnetic screening of protons by the magnetic Co_3O_4 core. Because the silica shells have a definite pore size (~4 nm), we hypothesized that the smaller EG monomer molecules should be able to penetrate the shell and continue to be impacted to a greater degree compared to the much larger Poly600 tridecamer molecules. To investigate this idea, the measured T_2 values were parametrized by dividing them over the unaffected, natural T_2 values (T_{2free}) of EG and Poly600 (measured in the absence of Co_3O_4; T_2/T_{2free} and 1 - T_2/T_{2free} in Figures 4c and 4d, respectively). After parametrization, it is clear that although the protons in both EG and Poly are relaxed by Co_3O_4, those in Poly600 are much more sensitive to the thickness of the silica shell.

We explain these observations as follows: With a hydrodynamic diameter of ∼1 nm,[72,73] the larger Poly600 molecules have much greater difficulty diffusing through the longer, more tortuous pathway needed to reach the magnetic Co_3O_4 core surface as the SiO_2 shell increases. In contrast, because the EG molecules are much smaller than the SiO_2 pores, thicker SiO_2 shells only slightly hinder the diffusion of EG molecules closer to the core. This results in a stronger T_2 shortening effect for EG.

Shorter diffusion pathways in Co_3O_4/porous SiO_2 particles with thinner shells allow molecular probes to move closer to the magnetic core. For the thinnest shells and the bare (uncoated) Co_3O_4 nanocrystals, small and large molecules are able to reach the magnetic surface and are affected equally. Together with the physisorption and TEM measurements presented above, these NMR experiments strongly suggest that that the surface of Co_3O_4 nanocrystals is accessible by small molecular substrates and reagents through a vast network of well-defined, ~4 nm pores. In contrast, the diffusion of large

DOI: 10.1021/cs501650j
ACS Catal. 2015, 5, 1037−1044

molecules such as Poly600 into the core region is hindered as their size becomes comparable with that of the pores. The porous silica shell thus serves as a sieve or filter for larger molecules.

Co_3O_4/SBA-15 Nanocomposites. Co_3O_4/SBA-15 nanocomposites were prepared by the sol−gel reaction between TEOS and H_2O, using HCl as catalyst and the block copolymer P123 as a structure-directing agent. The organic template was removed by calcination at 550 °C under air. Wet impregnation of cobalt(II) nitrate and calcination at 400 °C in air yielded Co_3O_4/SBA-15 nanocomposites with a nominal Co_3O_4 loading of 4 wt %. Further modification of the silica surface was conducted by postgrafting with various functional silanes (see the Experimental Section).

Low-angle XRD measurements show three peaks at 1.03°, 1.77°, and 2.01° corresponding to the (100), (110), and (200) planes in 2-D hexagonally packed SBA-15, respectively (Figure 5). The intensity of these three peaks remained unchanged after

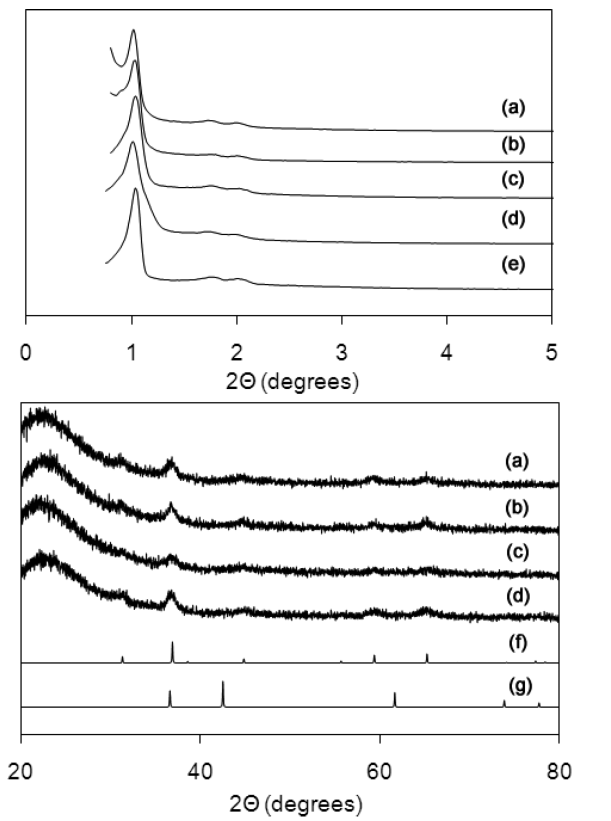

Figure 5. Low-angle (top) and wide-angle (bottom) powder XRD data for Co_3O_4/SBA-15 nanocomposites (4.4 ± 0.8 nm Co_3O_4 particle size): Co_3O_4/SBA-15/SiPh (a), Co_3O_4/SBA-15/$SiCH_2CH_2CH_2NH_2$ (b), Co_3O_4/SBA-15/$SiMe_3$ (c), Co_3O_4/SBA-15 (d), and SBA-15 (e). Bulk Co_3O_4 (f) and CoO (g) are shown for reference.

introduction of cobalt oxide, which suggests that the mesostructure of the SBA-15 support remained mostly intact. Wide-angle XRD measurements show that all modified (surface grafted) and unmodified Co_3O_4/SBA-15 nanocomposites contain standard spinel Co_3O_4 nanocrystals with a similar Scherrer particle size of 4.4 ± 0.8 nm (Figure 5). Nitrogen physisorption measurements show that, after the introduction of Co_3O_4, the surface area of Co_3O_4/SBA-15 nanocomposites dropped from 734 to 570 m^2/g, while the pore size remained nearly identical, from 6.5 to 6.4 nm. Postsynthetic grafting with silanes slightly decreased the surface area and also the pore size of the composites by up to 140 m^2/g and 0.6 nm, respectively (Table 2). It is noteworthy that the most dramatic decrease in

Table 2. Structural Data of SBA-15 and Co_3O_4/SBA-15 Nanocomposites

sample	S_{BET} (m^2/g)	pore size (nm)[a]	pore volume (cm^3/g)
SBA-15	730	6.5	0.95
Co_3O_4/SBA-15	570	6.4	0.91
Co_3O_4/SBA-15-$SiMe_3$	550	6.3	0.79
Co_3O_4/SBA-15-$SiCH_2CH_2CH_2NH_2$	430	5.8	0.70
Co_3O_4/SBA-15-SiPh	520	6.4	0.74

[a]Obtained by the BJH method.

surface area, pore size, and pore volume occurred in the amino ($-CH_2CH_2CH_2NH_2$)-modified specimen; however, no other significant changes in pore structure were observed in these surface modified Co_3O_4/SBA-15 composites. DP-MAS ^{29}Si NMR measurements were conducted to confirm the surface modification (Figure 6). New T bands (T^3 and T^2) are

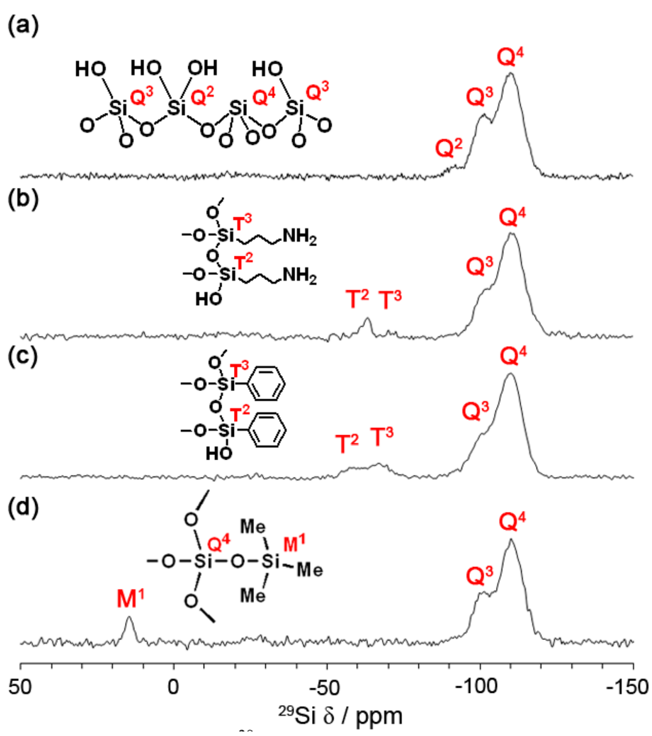

Figure 6. DP-MAS ^{29}Si NMR spectra of Co_3O_4/SBA-15 nanocomposites before (a) and after surface functionalization (by grafting) with $-(CH_2)_3NH_2$ (b), −Ph (c), and $-SiMe_3$ (d) groups.

observed for sites derived from $NH_2CH_2CH_2CH_2Si(OSi)_3$/$NH_2CH_2CH_2CH_2Si(OH)(OSi)_2$ and $PhSi(OSi)_3$/$PhSi(OH)(OSi)_2$ groups. A peak at ~15 ppm is observed for $Me_3Si(OSi)_3$ groups.[74−76]

Effect of Catalyst Microstructure on Water Oxidation. The catalytic activity of Co_3O_4/porous SiO_2 core/shell nanoparticles toward water oxidation was measured using a photosensitizer ($[Ru(bpy)_3]Cl_2·6H_2O$), a sacrificial electron acceptor ($Na_2S_2O_8-Na_2SO_4$), and an aqueous buffer (pH 5.8, $NaSiF_6-NaHCO_3$) medium. Reactions were conducted under

DOI: 10.1021/cs501650j
ACS Catal. 2015, 5, 1037−1044

continuous irradiation by 575 ± 100 nm lamps while taking aliquots of the headspace and injecting them into a GC equipped with a TCD detector to measure the oxygen (O_2) produced. Our setup (septum, etc.) was independently tested under similar conditions to ensure that there was no leakage or other noncatalytic sources of O_2.

The overall cycle for water oxidation under these conditions is shown in Scheme 1. $Ru(bpy)_3^{2+}$ is first excited by the

Scheme 1. Water Oxidation by $S_2O_8^{2-}$ Catalyzed by Co_3O_4/SiO_2 and $Ru(bpy)_3^{2+}$ (chloride salt) as Photosensitizer

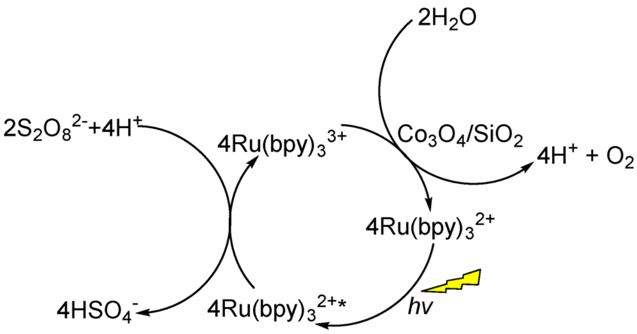

incident radiation to form an excited state, $Ru(bpy)_3^{2+*}$. Subsequent electron transfer from $Ru(bpy)_3^{2+*}$ to $S_2O_8^{2-}$ yields $Ru(bpy)_3^{3+}$ and $SO_4^{\bullet-}$. $SO_4^{\bullet-}$ further oxidizes another equivalent of $Ru(bpy)_3^{2+}$ to $Ru(bpy)_3^{3+}$. This $Ru(bpy)_3^{3+}$ reacts with water and oxidizes it on the surface of the Co_3O_4 catalyst, producing molecular oxygen (O_2). The free energy of the full process is calculated to be negative (exergonic or "downhill") and equal to −280 kJ/mol.

$$2H_2O \rightarrow O_2 + 4H^+ + 4e^- \qquad E_{red} = -1.23\ V$$
$$S_2O_8^{2-} + 4e^- \rightarrow 2SO_4^{2-} \qquad E_{ox} = 1.96\ V$$
$$2H_2O + 2S_2O_8^{2-} \rightarrow O_2 + 4H^+ + 4SO_4^{2-} \qquad E_{rxn} = 0.73\ V$$

$$\Delta G° = -nFE = -4 \times 96485\ C/mol \times 0.73\ V = -280\ kJ/mol$$

Figure 7 and Table 3 show the experimentally observed oxygen evolution activities of different Co_3O_4/porous SiO_2 nanocatalysts. In all cases, the amount of O_2 in the reactor headspace increased until reaching a plateau after 40−90 min. We interpret this plateau as the point at which the maximum yield of O_2 production in each case was achieved. Among the Co_3O_4/porous SiO_2 nanocatalysts studied, the bare, uncoated Co_3O_4 had the lowest activity. O_2 production then increased with increasing silica shell thickness up to a point; activity reached a maximum for Co_3O_4/porous SiO_2 with a 19.8 ± 1.4 nm shell, then decreased with a thicker shell (O_2 production activity was negligible in the absence of the nanocatalyst). We speculatively attribute this behavior to either one or both of two possible factors: (i) The positively charged $Ru(bpy)_3^{2+}$ photosensitizer may have a high affinity toward the negatively polarized SiO_2 surface. Thicker shells provide for a much larger SiO_2 surface (Table 1), increasing the effective concentration (and activity) of $Ru(bpy)_3^{2+}$ near or at the catalytically active Co_3O_4 surface. (ii) The porous silica coating could increase the effectiveness (rate of) electron transfer steps necessary for catalysis due to the lower permittivity (dielectric constant) of silica (3.9) compared with pure water (80). The lower permittivity could decrease the reorganizational energy term as described by Marcus theory, increasing the overall rate of electron transfer. The carrier mobility in 1-D and 2-D

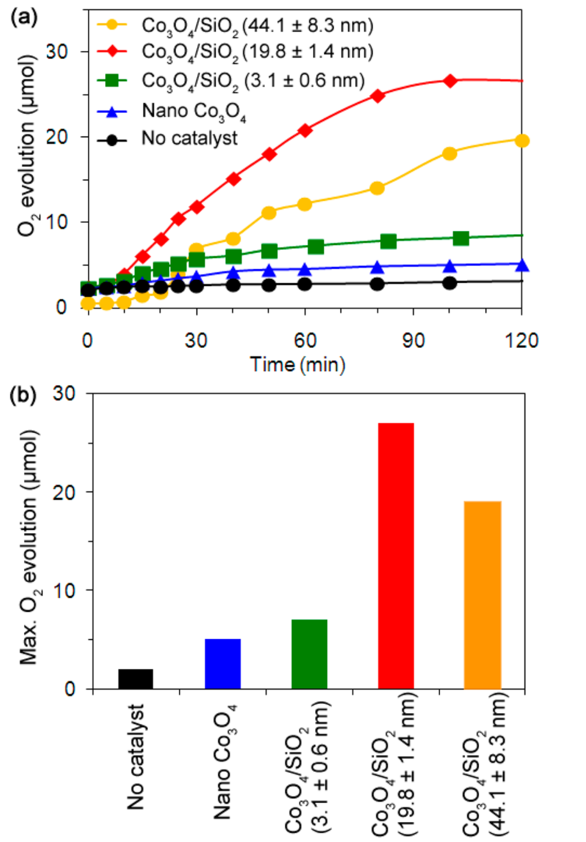

Figure 7. Oxygen evolution (a) and maximum O_2 yields (measured between 90 and 120 min, b) from the reaction of water with persulfate in the presence of $[Ru(bpy)_3]Cl_2$ sensitizer and Co_3O_4/SiO_2 core/shells under 575 ± 100 nm lamp illumination (the total Co_3O_4 loading and concentration were maintained constant).

Table 3. Maximum Oxygen Evolution Performance of Co_3O_4/Porous SiO_2 Nanocatalysts

sample	oxygen evolved (μmol)	yield (%)
Co_3O_4	5.2	3.8
Co_3O_4/SiO_2 (3 nm)[a]	8.7	6.4
Co_3O_4/SiO_2 (20 nm)[a]	26.7	19.6
Co_3O_4/SiO_2 (44 nm)[a]	19.8	14.5
Co_3O_4/SBA-15	28.5	20.8
Co_3O_4/SBA-15/$SiMe_3$	20.4	15.0
Co_3O_4/SBA-15/$SiCH_2CH_2CH_2NH_2$	15.4	11.3
Co_3O_4/SBA-15/SiPh	19.4	14.2

[a]Approximate shell thickness (as in Table 1).

semiconductor nanostructures is sensitive to permittivity,[77] as is that of single-layer graphene transistors in different dielectric environments.[78,79]

The catalytic activities of surface-modified and unmodified Co_3O_4/SBA-15 nanocomposites were also measured for comparison (Figure 8 and Table 3). The concentration of O_2 produced using Co_3O_4/SBA-15 nanocomposites reached a maximum yield within 50−60 min, which is consistent with the aforementioned and with prior reports.[22,44] Interestingly, among the composite catalysts, it is the unmodified sample that possesses the best performance, whereas the other three modified samples possessed lower, similar activities. The composites containing the most hydrophobic surface groups (−SiPh and −$SiMe_3$) and thus, a low permittivity, show

DOI: 10.1021/cs501650j
ACS Catal. 2015, 5, 1037−1044

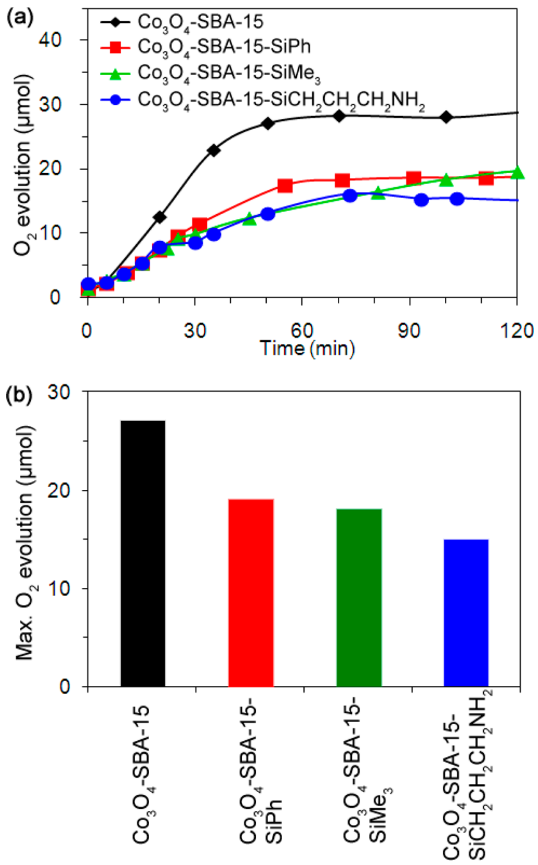

Figure 8. Oxygen evolution (a) and maximum O_2 yields (measured between 60 and 120 min, b) from the reaction of water with persulfate in the presence of $[Ru(bpy)_3]Cl_2$ sensitizer and Co_3O_4/SBA-15 nanocomposites under 575 ± 100 nm lamp illumination (the total Co_3O_4 loading and concentration were maintained constant).

relatively low activity, arguing against factor ii, above. More generally, however, we believe that the decrease in activity in the surface-grafted composites is most likely attributable to a decrease in the SiO_2 surface available for binding by the $Ru(bpy)_3^{2+}$ photosensitizer (roughly opposite to factor i, mentioned above), as indicated by physisorption measurements (Table 2); albeit, this could be compensated somewhat by the introduction of surface $-NH_2$ groups in one of the nanocomposites.

CONCLUSION

We have prepared several Co_3O_4/porous silica nanocomposites to investigate the effect of catalyst microstructure and its local environment on water oxidation activity. We have also utilized NMR relaxation time measurements of two different probe molecules (EG and Poly600) to study the pore accessibility of Co_3O_4/porous SiO_2 core/shell nanoparticles with different shell thicknesses (but similar pore size and structure).

In our study of catalytic activity of Co_3O_4/porous SiO_2 core/shell nanoparticles toward water oxidation (oxygen evolution reaction), the catalyst with a 19.8 ± 1.4 nm shell had superior activity over the uncoated, thinner, and thicker silica shell catalysts as a result of two possible factors: First, the higher surface area of the thicker porous silica shell helps to increase the local $Ru(bpy)_3^{2+}$ concentration near the active Co_3O_4 surface. Second, the reduced reorganization energy due to the lower dielectric constant of silica might also facilitate the charge transfer rate. Increasing shell thicknesses were detrimental to catalytic activity, possibly because of slower diffusion of reactant molecules in and out of the SiO_2 pores.

In the case of Co_3O_4/SBA-15 nanocomposites, the unmodified sample possesses better activity than the modified samples. Surface-modified composites (e.g., −SiPh and $-SiMe_3$) have relatively low local surface permittivity compared with the unmodified composites; however, the loss of possible $Ru(bpy)_3^{2+}$ binding sites (hydroxyl group) and a measurable amount of pore blocking upon surface grafting results in the loss of reactivity. A more thorough understanding of the effects of microstructure and permittivity on water oxidation ability will enable the construction of next generation catalysts possessing optimal configuration and better efficiency for water oxidation and water splitting.

ASSOCIATED CONTENT

Supporting Information

The following file is available free of charge on the ACS Publications website at DOI: 10.1021/cs501650j

Absorption and irradiance profiles of catalyst, sensitizer, and lamp. ICP-MS and colorimetric analyses of Co content in all materials studied (PDF)

AUTHOR INFORMATION

Corresponding Author

*E-mail: vela@iastate.edu.

Notes

The authors declare no competing financial interest.

ACKNOWLEDGMENTS

J. Vela gratefully acknowledges the National Science Foundation for funding of this work through the Division of Materials Research, Solid State and Materials Chemistry program (NSF-DMR-1309510). The authors thank Sarah Cady for assistance with NMR, Jenee Jacobs and Sam Houk for assistance with ICP-MS, and Michelle Thompson for comments.

REFERENCES

(1) Yan, Y.; Xia, B. Y.; Xu, Z.; Wang, X. *ACS Catal.* **2014**, *4*, 1693−1705.
(2) Deng, X.; Tüysüz, H. *ACS Catal.* **2014**, *4*, 3701−3714.
(3) Maeda, K.; Domen, K. *J. Phys. Chem. Lett.* **2010**, *1*, 2655−2661.
(4) Cook, T. R.; Dogutan, D. K.; Reece, S. Y.; Surendranath, Y.; Teets, T. S.; Nocera, D. G. *Chem. Rev.* **2010**, *110*, 6474−6502.
(5) Inoue, H.; Shimada, T.; Kou, Y.; Nabetani, Y.; Masui, D.; Takagi, S.; Tachibana, H. *ChemSusChem* **2011**, *4*, 173−179.
(6) Nocera, D. G. *Acc. Chem. Res.* **2012**, *45*, 767−776.
(7) Reece, S. Y.; Hamel, J. A.; Sung, K.; Jarvi, T. D.; Esswein, A. J.; Pijpers, J. J. H.; Nocera, D. G. *Science* **2011**, *334*, 645−648.
(8) Artero, V.; Chavarot-Kerlidou, M.; Fontecave, M. *Angew. Chem., Int. Ed.* **2011**, *50*, 7238−7266.
(9) Chou, N. H.; Ross, P. N.; Bell, A. T.; Tilley, T. D. *ChemSusChem* **2011**, *4*, 1566−1569.
(10) Esswein, J.; McMurdo, M. J.; Ross, P. N.; Bell, A. T.; Tilley, T. D. *J. Phys. Chem. C* **2009**, *113*, 15068−15072.
(11) Gerken, J. B.; McAlpin, J. G.; Chen, J. Y. C.; Rigsby, M. L.; Casey, W. H.; Britt, R. D.; Stahl, S. S. *J. Am. Chem. Soc.* **2011**, *133*, 14431−14442.
(12) Yeo, B. S.; Bell, A. T. *J. Am. Chem. Soc.* **2011**, *133*, 5587−5593.
(13) Liang, Y.; Li, Y.; Wang, H.; Zhou, J.; Wang, J.; Regier, T.; Dai, H. *Nat. Mater.* **2011**, *10*, 780−786.

(14) Liao, M.; Feng, J.; Luo, W.; Wang, Z.; Zhang, J.; Li, Z.; Yu, T.; Zou, Z. *Adv. Funct. Mater.* **2012**, *22*, 3066−3074.
(15) Hou, J.; Wang, Z.; Yang, C.; Cheng, H.; Jiao, S.; Zhu, H. *Energy Environ. Sci.* **2013**, *6*, 3322−3330.
(16) Kent, C. A.; Concepción, J. J.; Dares, C. J.; Torelli, D. A.; Rieth, A. J.; Miller, A. S.; Hoertz, P. G.; Meyer, T. J. *J. Am. Chem. Soc.* **2013**, *135*, 8432−8435.
(17) Surendranath, Y.; Lutterman, D. A.; Liu, Y.; Nocera, D. G. *J. Am. Chem. Soc.* **2012**, *134*, 6326−6336.
(18) Wee, T.-L.; Sherman, B. D.; Gust, D.; Moore, A. L.; Moore, T. A.; Liu, Y.; Scaiano, J. C. *J. Am. Chem. Soc.* **2011**, *133*, 16742−16745.
(19) Sa, Y. J.; Kwon, K.; Cheon, J. Y.; Kleitz, F.; Joo, S. H. *J. Mater. Chem. A* **2013**, *1*, 9992−10001.
(20) Grewe, T.; Deng, X.; Weidenthaler, C.; Schüth, F. *Chem. Mater.* **2013**, *25*, 4926−4935.
(21) Grewe, T.; Deng, X.; Tüysüz, H. *Chem. Mater.* **2014**, *26*, 3162−3168.
(22) Jiao, F.; Frei, H. *Chem. Commun.* **2010**, *46*, 2920−2922.
(23) Jiao, F.; Frei, H. *Energy Environ. Sci.* **2010**, *3*, 1018−1027.
(24) Hara, M.; Waraksa, C. C.; Lean, J. T.; Lewis, B. A.; Mallouk, T. E. *J. Phys. Chem. A* **2000**, *104*, 5275−5280.
(25) Boppana, V. B. R.; Jiao, F. *Chem. Commun.* **2011**, *47*, 8973−8975.
(26) Iyer, A.; Del-Pilar, J.; King'ondu, C. K.; Kissel, E.; Garces, H. F.; Huang, H.; El-Sawy, A. M.; Dutta, P. K.; Suib, S. L. *J. Phys. Chem. C* **2012**, *116*, 6474−6483.
(27) Wei, J.; Liu, Y.; Ding, Y.; Luo, C.; Du, X.; Lin, J. *Chem. Commun.* **2014**, *50*, 11938−11941.
(28) Yamada, Y.; Yano, K.; Hong, D.; Fukuzumi, S. *Phys. Chem. Chem. Phys.* **2012**, *14*, 5753−5760.
(29) Najafpour, M. M.; Ehrenberg, T.; Wiechen, M.; Kurz, P. *Angew. Chem., Int. Ed.* **2010**, *49*, 2233−2237.
(30) Conrad, F.; Bauer, M.; Sheptyakov, D.; Weyeneth, S.; Jaeger, D.; Hametner, K.; Car, P.-E.; Patscheider, J.; Günther, D.; Patzke, G. R. *RSC Adv.* **2012**, *2*, 3076−3082.
(31) Shevchenko, D.; Anderlund, M. F.; Thapper, A.; Styring, S. *Energy Environ. Sci.* **2011**, *4*, 1284−1287.
(32) Gardner, G. P.; Go, Y. B.; Robinson, D. M.; Smith, P. F.; Hadermann, J.; Abakumov, A.; Greenblatt, M.; Dismukes, G. C. *Angew. Chem., Int. Ed.* **2012**, *51*, 1616−1619.
(33) Hong, D.; Yamada, Y.; Nagatomi, T.; Takai, Y.; Fukuzumi, S. *J. Am. Chem. Soc.* **2012**, *134*, 19572−19575.
(34) Yin, Q.; Tan, J. M.; Besson, C.; Geletti, Y. V.; Musaev, D. G.; Kuznetsov, A. E.; Luo, Z.; Hardcastle, K. I.; Hill, C. L. *Science* **2010**, *328*, 342−345.
(35) Huang, Z.; Luo, Z.; Geletii, Y. V.; Vickers, J. W.; Yin, Q.; Wu, D.; Hou, Y.; Ding, Y.; Song, J.; Musaev, D. G.; Hill, C. L.; Lian, T. *J. Am. Chem. Soc.* **2011**, *133*, 2068−2071.
(36) Vickers, J. W.; Lv, H.; Sumliner, J. M.; Zhu, G.; Luo, Z.; Musaev, D. G.; Geletii, Y. V.; Hill, C. L. *J. Am. Chem. Soc.* **2013**, *135*, 14110−14118.
(37) Lv, H.; Song, J.; Geletii, Y. V.; Vickers, J. W.; Sumliner, J. M.; Musaev, D. G.; Kögerler, P.; Zhuk, P. F.; Bacsa, J.; Zhu, G.; Hill, G. L. *J. Am. Chem. Soc.* **2014**, *136*, 9268−9271.
(38) Stracke, J. J.; Finke, R. G. *J. Am. Chem. Soc.* **2011**, *133*, 14872−14875.
(39) Stracke, J. J.; Finke, R. G. *ACS Catal.* **2014**, *4*, 79−89.
(40) Hong, D.; Jung, J.; Park, J.; Yamada, Y.; Suenobu, T.; Lee, Y.-M.; Nam, W.; Fukuzumi, S. *Energy Environ. Sci.* **2012**, *5*, 7606−7616.
(41) Zidki, T.; Zhang, L.; Shafirovich, V.; Lymar, S. V. *J. Am. Chem. Soc.* **2012**, *134*, 14275−14278.
(42) McCool, N. S.; Robinson, D. M.; Sheats, J. E.; Dismukes, G. C. *J. Am. Chem. Soc.* **2011**, *133*, 11446−11449.
(43) Berardi, S.; La Ganga, G.; Natali, M.; Bazzan, I.; Puntoriero, F.; Sartorel, A.; Scandola, F.; Campagna, S.; Bonchio, M. *J. Am. Chem. Soc.* **2012**, *134*, 11104−11107.
(44) Jiao, F.; Frei, H. *Angew. Chem., Int. Ed.* **2009**, *48*, 1841−1844.
(45) Grzelczak, M.; Zhang, J.; Pfrommer, J.; Hartmann, J.; Driess, M.; Antonietti, M.; Wang, X. *ACS Catal.* **2013**, *3*, 383−388.
(46) Yang, C.-C.; Eggenhusien, T. M.; Wolters, M.; Agiral, A.; Frei, H.; de Jongh, P. E.; de Jong, K. P.; Mul, G. *ChemCatChem.* **2013**, *5*, 550−556.
(47) Yusuf, S.; Jiao, F. *ACS Catal.* **2012**, *2*, 2753−2760.
(48) Rosen, J.; Hutchings, G. S.; Jiao, F. *J. Am. Chem. Soc.* **2013**, *135*, 4516−4521.
(49) Zhang, Y.; Rosen, J.; Hutchings, G. S.; Jiao, F. *Catal. Today* **2014**, *225*, 171−176.
(50) Ahn, H. S.; Yano, J.; Tilley, T. D. *Energy Environ. Sci.* **2013**, *6*, 3080−3087.
(51) Del Pilar-Albaladejo, J.; Dutta, P. K. *ACS Catal.* **2014**, *4*, 9−15.
(52) Armandi, M.; Hernandez, S.; Vankova, S.; Zaranilli, S.; Boneli, B.; Garrone, E. *ACS Catal.* **2013**, *3*, 1272−1278.
(53) Zhao, J.; Zou, Y.; Zou, X.; Bai, T.; Liu, Y.; Gao, R.; Wang, D.; Li, G.-D. *Nanoscale* **2014**, *6*, 7255−7262.
(54) Zhou, L.-J.; Zou, Y.; Li, G.-D.; Zou, X.; Zhao, J.; Fan, M.; Liu, Y.; Wang, D. *RSC Adv.* **2014**, *4*, 22951−22954.
(55) Soo, H. S.; Agiral, A.; Bachmeier, A.; Frei, H. *J. Am. Chem. Soc.* **2012**, *134*, 17104−17116.
(56) Agiral, A.; Soo, H. S.; Frei, H. *Chem. Mater.* **2013**, *25*, 2264−2273.
(57) Mavros, M. G.; Tsuchimochi, T.; Kowalczyk, T.; McIsaac, A.; Wang, L.-P.; Van Voorhis, T. *Inorg. Chem.* **2014**, *53*, 6386−6397.
(58) Kwapien, K.; Piccinin, S.; Fabris, S. *J. Phys. Chem. Lett.* **2013**, *4*, 4223−4230.
(59) Chen, J.; Selloni, A. *J. Phys. Chem. Lett.* **2012**, *3*, 2808−2814.
(60) Luisetto, I.; Pepe, F.; Bemporad, E. *J. Nanopart. Res.* **2008**, *10*, 59−67.
(61) Meng, Y.; Chen, D.; Jiao, X. *J. Phys. Chem. B* **2006**, *110*, 15212−15217.
(62) Deng, Y.; Qi, D.; Deng, C.; Zhang, X.; Zhao, D. *J. Am. Chem. Soc.* **2008**, *130*, 28−29.
(63) Deng, Y.; Cai, Y.; Sun, Z.; Liu, J.; Liu, C.; Wei, J.; Li, W.; Liu, C.; Wang, Y.; Zhao, D. *J. Am. Chem. Soc.* **2010**, *132*, 8466−8473.
(64) Choi, M.; Heo, W.; Kleitz, F.; Ryoo, R. *Chem. Commun.* **2003**, 1340−1341.
(65) Sharma, K. K.; Buckley, R. P.; Asefa, T. *Langmuir* **2008**, *24*, 14306−14320.
(66) Xu, R.; Zeng, H. C. *Langmuir* **2004**, *20*, 9780−9790.
(67) Olguin, G.; Yacou, C.; Smart, S.; da Costa, J. C. D. *Sci. Rep.* **2013**, *3*, 2449-1−5.
(68) Khodakov, A. Y.; Chu, W.; Fongarland, P. *Chem. Rev.* **2007**, *107*, 1692−1744.
(69) Gillis, P.; Moiny, F.; Brooks, R. A. *Magn. Reson. Med.* **2002**, *47*, 257−263.
(70) Pinho, S. L. C.; Pereira, G. A.; Voisin, P.; Kassem, J.; Bouchaud, V.; Etienne, L.; Peters, J. A.; Carlos, L.; Mornet, S.; Geraldes, C. F. G. C.; Rocha, J.; Delville, M.-H. *ACS Nano* **2010**, *4*, 5339−5349.
(71) Paquet, C.; de Haan, H. W.; Leek, D. M.; Lin, H.-Y.; Xiang, B.; Tian, G.; Kell, A.; Simard, B. *ACS Nano* **2011**, *5*, 3104−3112.
(72) Armstrong, J. K.; Wenby, R. B.; Meiselman, H. J.; Fisher, T. C. *Biophys. J.* **2004**, *87*, 4259−4270.
(73) Dohmen, M. P. J.; Pereira, A. M.; Timmer, J. M. K.; Benes, N. E.; Keurentjes, J. T. F. *J. Chem. Eng. Data* **2008**, *53*, 63−65.
(74) Díaz, U.; García, T.; Velty, A.; Corma, A. *J. Mater. Chem.* **2009**, *19*, 5970−5979.
(75) Williams, E. A. In *The Chemistry of Organic Silicon Compounds*; Patai, S., Rappoport, Z., Eds.; John Willey & Sons: New York, 1989; p 511.
(76) Uhlig, F.; Marsmann, H. C. In *Gelest Catalog: Silicon Compounds, Silanes & Silicones*, 2nd ed.; Arkles, B., Larson, G., Eds.; Gelest: Morrisville, PA, 2008; p 208.
(77) Jena, D.; Konar, A. *Phys. Rev. Lett.* **2007**, *98*, 136805.
(78) Konar, A.; Fang, T.; Jena, D. *Phys. Rev. B* **2010**, *82*, 115452.
(79) Hollander, M. J.; LaBella, M.; Hughes, Z. R.; Zhu, M.; Trumbull, K. A.; Cavalero, R.; Snyder, D. W.; Wang, X. J.; Hwang, E.; Datta, S.; Robinson, J. A. *Nano Lett.* **2011**, *11*, 3601−3607.

DOI: 10.1021/cs501650j
ACS Catal. 2015, 5, 1037−1044